Seventh International Conference on Computational Fluid Dynamics (ICCFD7), Big Island, Hawaii, July 9-13, 2012

ICCFD7-2401

EGO Method for Diffusing S-duct Shape Design

Hyo Gil Bae*, Soo Hyung Park** and Jank Hyuk Kwon*
Corresponding author: jhkwon@kaist.ac.kr

* Department of Aerospace Engineering, Korea Advanced Institute of Science and Technology, Republic of Korea
** Department of Aerospace Information Engineering, Konkuk University, Seoul, Republic of Korea

Abstract: The efficient global optimization (EGO) method is a global optimization technique based on the stochastic kriging model to efficiently search the global optimum in a design space. EGO selects the next sample point in the view of the probability that a global minimum is located. To present the probability the EGO method uses the infill sampling criteria (ISC) functions. The ISC is defined with the mean and variance at the untried point provided from the kriging model. The EGO method was applied to a diffusing S-duct shape design problem which needs a computationally expensive turbulent computational fluid dynamics (CFD) analysis. Also the penalized imputation method was considered to handle the conditions at which the CFD solution was not converged. Our results confirmed that the improved S-duct shape was searched globally and efficiently through the EGO method. And the effectiveness of EGO method was shown comparing with a gradient-based optimization

Keywords: Kriging model, Efficient global optimization (EGO), Infill sampling criteria (ISC), Penalized imputation, S-duct

1 Introduction

The diffusing S-duct is a typical aircraft inlet geometry. It decelerates air entering the compressor and increases the static pressure. The Lockheed Martin F-16 has a chin-type S-duct and Korean advanced supersonic trainer T-50 has a bifurcated S-duct.

A well designed diffusing S-duct can help to enhance engine performance by delivering a nearly uniform flow with a small transverse velocity component at the engine compressor entrance. But the centerline curvature associated with the S-duct determines the centrifugal force and cross-stream pressure gradient between the bottom and the top of S-duct. As a result the diffusing S-duct integrates the complex 3-dimensional internal flow which includes secondary flows and flow separation. Wellborn et al. [1] performed a compressible subsonic flow experiment through a representative S-duct configuration and investigated the complicated flow mechanism in detail. The baseline diffuser of our design corresponds to the experimental configuration of Wellborn et al.

The aerodynamic performance of subsonic diffusers is principally determined by two parameters; the flow distortion at the outlet of the diffuser and the total pressure recovery. If the flow distortion is reduced and the total pressure recovery is close to one, it can be considered to be well-designed.

To estimate performance characteristics of an S-duct without experiments, computational studies have been done with different turbulent models. Harloff et al. [2] used the PARC3D [3] computer program to solve the full, three-dimensional Reynolds-averaged Navier-Stokes equations. Harloff et al. computed a subsonic S-duct flow using the Baldwin-Lomax algebraic turbulence model and the k-ε turbulent model. Zhang et al. [4] performed computational analysis of the S-duct diffuser by utilizing the Baldwin-Lomax turbulent algebraic model. Details are presented by Zhang [5]. Lee and Kim [7] analyzed the S-duct computationally and concluded that the k-ω shear stress transport (SST) two equation turbulent model predicts the flow characteristics better than Spalart-Allmaras and k-ω models.

For the optimization method of S-duct shape, the sequential quadratic programming (SQP) [4,6] and the adjoint equations [7] were used. Both are gradient-based optimizers. The multi-objective genetic algorithm (MOGA) was also used as a global search method [8]. Generally gradient-based optimization methods provide an accurate local minimum in the design space, but such optimization requires sensitivity information to calculate the search direction. Using the adjoint equations [7], the sensitivity can be computed at once irrespective of the number of design variables. However, applying the adjoint equation to a specific analysis code is still limited for engineers to use in the field. The genetic algorithm also has the demerit of requiring a lot of evaluating function.

Thus, surrogate-based optimization has become a noteworthy method [9,10] nowadays. With a surrogate model, the global minimum can be searched for by looking at and investigating the design space, and the surrogate model can be constructed with a few analysis runs. Another advantage is that previously analyzed data can be reused to build a surrogate model later after it has been stored. However, the difficulty of surrogate-based optimization is in selecting the next sample point that can cover the local and global searches in the design space.

For this reason, Jones et al. [11] developed the efficient global optimization (EGO) method based on the stochastic kriging model. EGO selects the next sample point that has the maximum probability that the global minimum exists. The probability is expressed by the mean value and the variance of the kriging model. The uncertainty (=variance) of the kriging model at untried points is considered as not a risk but an opportunity to search for a good solution. The functions such as probability to use to select the next sample point are called infill sampling criteria (ISC). Because the EGO method needs a minimal number of analysis runs to search a global minimum, the EGO method can be a good way for optimization when the analysis is computationally expensive such as in a CFD analysis.

The objective of this study is to apply the EGO method to the diffusing S-duct shape design and to investigate the effectiveness of the EGO method comparing with the result of gradient-based optimization.

2 Efficient Global Optimization

2.1 Kriging model

The EGO method is based on the stochastic kriging model. The true function $\mathrm{Y}(\mathbf{x})$ is assumed to be comprised of a regression model $\mathbf{f}(\mathbf{x})^{\mathbf{T}}\boldsymbol{\beta}$ and stochastic departure model $\mathrm{Z}(\mathbf{x})$. The regression model covers the design space globally but the departure model expresses the design space locally [12].

$$\mathrm{Y}(\mathbf{x}) = \mathbf{f}(\mathbf{x})^{\mathbf{T}}\boldsymbol{\beta} + Z(\mathbf{x}) \tag{1}$$

where $\mathbf{x}$ is the design variable vector, $\mathbf{f}(\mathbf{x})$ is the vector of regression functions, and $\boldsymbol{\beta}$ is the vector of unknown coefficients.

It can be assumed that departure terms are correlated with each other when doing a computer experiment because the computer experiment is deterministic and does not have measurement error

and noise. In the kriging model the covariance between departures $Z(\mathbf{s}_i)$ and $Z(\mathbf{s}_j)$ at sample points is assumed to be expressed as the product of process variance σ_z^2 and correlation matrix **R.**

$$\mathrm{cov}[Z(\mathbf{s}_i), Z(\mathbf{s}_j)] \equiv \sigma_z^2 \mathbf{R} \tag{2}$$

The correlation matrix consists of the spatial correlation function R such as equation (3)**.** When the distance between the points is large, the function will be zero. On the other hand, when the distance between the points is small, the function will become near one.

$$R(\boldsymbol{\theta}, \mathbf{s}_i, \mathbf{s}_j) = \exp[-\sum_{k=1}^{dv} \theta_k |s_{i,k} - s_{j,k}|^2] \tag{3}$$

where i,j=1,⋯ , n is the number of sample points, s is the coordinate of sample points, k is the number of design variables and θ is the correlation parameter.

Using the properties of the Best Linear Unbiased Predictor (BLUP), the kriging model is completed. The mean square error (MSE) of prediction is minimized by introducing Lagrange multipliers and unbiasedness constraints. Thus, the kriging model $\hat{Y}(\mathbf{x})$ is derived in equation (4). The kriging model also is called Design and Analysis of Computer Experiments (DACE) predictor [13].

$$\hat{Y}(\mathbf{x}) = \mathbf{f}(\mathbf{x})^T \hat{\boldsymbol{\beta}} + \mathbf{r}(\mathbf{x})^T \mathbf{R}^{-1} (\mathbf{Y} - \mathbf{F}\hat{\boldsymbol{\beta}}) \tag{4}$$

$$\mathbf{r}(\mathbf{x}) = [R(\boldsymbol{\theta}, \mathbf{x}, \mathbf{s}_1), R(\boldsymbol{\theta}, \mathbf{x}, \mathbf{s}_2), \cdots, R(\boldsymbol{\theta}, \mathbf{x}, \mathbf{s}_n)]^T \tag{5}$$

$$\hat{\boldsymbol{\beta}} = (\mathbf{F}^T \mathbf{R}^{-1} \mathbf{F})^{-1} \mathbf{F}^T \mathbf{R}^{-1} \mathbf{Y} \tag{6}$$

where $\mathbf{r}(\mathbf{x})$ is the correlation vector between the untried point $\mathbf{x}$ and the sample point $\mathbf{s}$, $\hat{\boldsymbol{\beta}}$ is the generalized least square estimation, and $\mathbf{F}$ is the matrix of the regression function.

The MSE of the predictor also is derived in equation (7).

$$\mathrm{MSE}[\hat{Y}(\mathbf{x})] = \hat{s}^2 = \sigma_z^2 \left(1 - \mathbf{r}^T \mathbf{R}^{-1} \mathbf{r} + \mathbf{u}^T (\mathbf{F}^T \mathbf{R}^{-1} \mathbf{F})^{-1} \mathbf{u}\right) \tag{7}$$

$$\sigma_z^2 = (\mathbf{Y} - \mathbf{F}\hat{\boldsymbol{\beta}})^T \mathbf{R}^{-1} (\mathbf{Y} - \mathbf{F}\hat{\boldsymbol{\beta}})/n \tag{8}$$

$$\mathbf{u} = \mathbf{F}^T \mathbf{R}^{-1} \mathbf{r}(\mathbf{x}) - \mathbf{f}(\mathbf{x}) \tag{9}$$

With equations (8) and (9) above, the correlation parameter vector $\boldsymbol{\theta}$ is still unknown. In the kriging model the maximum likelihood estimation (MLE) is used to estimate the correlation parameters. Because the response Y is assumed to have Gausssian distribution, the likelihood function to determine the correlation parameter is defined as equation (10) [23].

$$L \equiv \frac{1}{(2\pi)^{n/2} \sqrt{|\sigma_z^2 \mathbf{R}|}} \exp\left[\frac{-(\mathbf{Y} - \mathbf{F}\hat{\boldsymbol{\beta}})^T \mathbf{R}^{-1} (\mathbf{Y} - \mathbf{F}\hat{\boldsymbol{\beta}})}{2\sigma_z^2}\right] \tag{10}$$

Finally the MLE is converted to a minimization problem of non-logarithm form as equation (9) [12]. The correlation parameter is determined by minimizing this likelihood function.

$$\min_{\theta} \sigma_z^2 |R|^{1/n} \tag{11}$$

In this study, the kriging code implementation was based on the Simpson [15] Fortran program and had sophisticated numerical techniques (Cholesky decomposition, QR factorization, the nugget effect, and avoiding underflow) [16].

2.2 EGO method

The process of EGO method is plotted in Fig. 1. Differently from the original surrogate-based optimization, the EGO method selects the next sample point not using the kriging model directly but using the infill sampling criteria (ISC) function. The ISC function is determined considering the predictor (=mean) and the mean square error (=variance) which are provided from the kriging model. One of ISC, the EGO usually uses the expected improvement (EI) function like the equation (14). The EI function is derived from the improvement function I in order to express the probability that the next sample would be less than the current minimum. The current minimum f_{min} is obtained based on the sampled points so far.

$$I = \max[(f_{min} - Y(\mathbf{x})), 0] \tag{12}$$
$$Y(\mathbf{x}) \sim N(\hat{Y}(\mathbf{x}), \hat{s}^2(\mathbf{x})) \tag{13}$$

where $Y(\mathbf{x})$ is the true function assuming the normal distribution random variable model. By the probability technique, the expected value of the improvement function is calculated as given in equation (14).

$$E[I(x)] = \begin{cases} (f_{min} - \hat{Y})\Phi\left(\frac{f_{min} - \hat{Y}}{\hat{s}}\right) + \hat{s}\phi\left(\frac{f_{min} - \hat{Y}}{\hat{s}}\right) & if\ \hat{s} > 0 \\ 0 & if\ \hat{s} = 0 \end{cases} \tag{14}$$

where $\Phi(\cdot)$ and $\phi(\cdot)$ denote the standard normal cumulative distribution function (CDF) and the probability density function (PDF). The first term is the difference between the current minimum and the predicted value multiplied by the probability that the random variable $Y(\mathbf{x})$ is smaller than f_{min}. The first term is large where $\hat{Y}$ is likely smaller than f_{min}. The second term tends to be large where there is a high uncertainty (=variance). Thus the EGO method selects the next sample point that has the maximum expected improvement (EI) value for both regions of improvement and regions of high uncertainty [14]. Then the kriging model is updated with the selected next sample point. As EGO samples the next point close to the optimum, EI is gradually reduced.

In this study, another ISC function WB2 was considered [14]. It is the combination of kriging predictor and EI function as given in equation (15). The negative sign in front of $\hat{Y}$ is to make the problem maximize corresponding to EI. Thus the EGO method selects the next sample point that has the maximum WB2 value in the design space. WB2 has known to have the exploitation performance superior to EI because it consists of the kriging predictor $\hat{Y}$ itself.

$$WB2 = \begin{cases} -\hat{Y} + (f_{min} - \hat{Y})\Phi\left(\frac{f_{min} - \hat{Y}}{\hat{s}}\right) + \hat{s}\phi\left(\frac{f_{min} - \hat{Y}}{\hat{s}}\right) & if\ \hat{s} > 0 \\ 0 & if\ \hat{s} = 0 \end{cases} \tag{15}$$

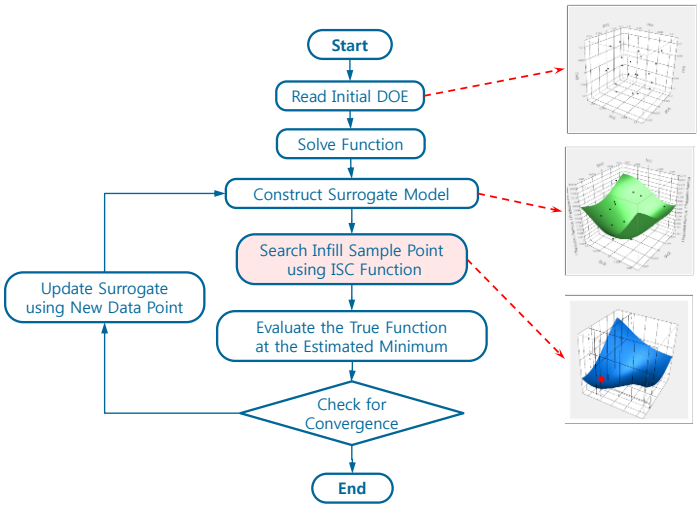

Fig. 1 Flow chart of EGO

2.3 Penalized imputation

During the design process with an analysis code, unusual situations can happen. For example, (i) the geometry described by design variables may be twisted, (ii) an automated grid generator may fail to make a mesh for a complex geometry, (iii) the analysis code may not converge due to a bad mesh or an unusual configuration. To cope with these problems, the penalized imputation method was proposed by A. Forrester [22,24]. The point at which the unusual situation occurs is called the infeasible point. The analyzed value at the infeasible point in the design space is not used to make the kriging model. Instead the kriging model is constructed with only feasible points. Then the analyzed value at the infeasible point is replaced with the penalized imputed value as given equation (16). Adding the mean square error $\hat{s}^2$ means to be penalized.

$$\text{Infeasible point} \leftarrow \hat{Y} + \hat{s}^2 \tag{16}$$

Using feasible points and penalized imputed points, the kriging model is constructed again so that the EGO method can select the next sample point with that kriging model. The EGO method with the penalized imputation is explained in Fig. 2.

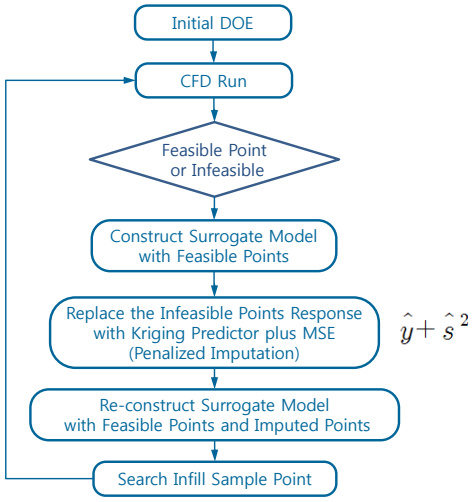

Fig. 2 Flow chart of penalized imputation

3 Diffusing S-duct CFD Analysis

3.1 Geometry of S-duct

The geometry of the diffusing S-duct is shown in Fig. 3. The duct centerline (cl) is defined by two planar circular arcs with identical radii, R of 102.1 cm and subtended angles, $\theta_{max}/2$ of 30°. The centerline coordinates, given by equation (17), are indicated by the dashed line in Fig. 3. All cross sections (plane A,B,C,D,E) perpendicular to the centerline are circular. The duct inlet radius, r_1 is 10.21 cm. The duct outlet radius, r_2 is 12.57 cm, which produced an area ratio, A_1/A_2 of 1.52. The variation of the duct radius as a function of the angle θ is given by equation (18).

$$\begin{aligned}
&\text{For } 0 \le \theta \le \theta_{max}/2 \\
&\quad x_{cl} = R\sin\theta \\
&\quad y_{cl} = 0 \\
&\quad z_{cl} = R\cos\theta - R \\
&\text{For } \theta_{max}/2 \le \theta \le \theta_{max} \\
&\quad x_{cl} = 2R\sin(\theta_{max}/2) - R\sin(\theta_{max} - \theta) \\
&\quad y_{cl} = 0 \\
&\quad z_{cl} = 2R\cos(\theta_{max}/2) - R - R\cos(\theta_{max} - \theta)
\end{aligned} \tag{17}$$

$$r/r_1 = 1 + 3(r_2/r_1 - 1)\,(\theta/\theta_{max})^2 - 2(r_2/r_1 - 1)\,(\theta/\theta_{max})^3 \tag{18}$$

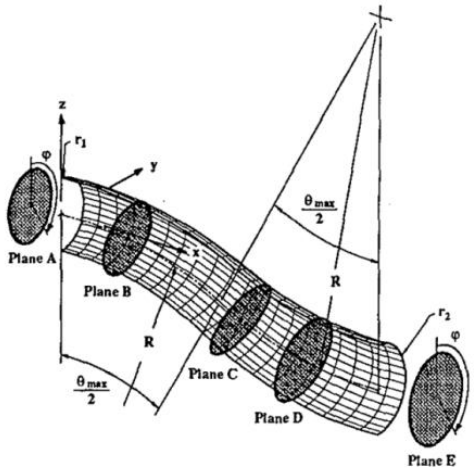

Fig. 3 Baseline S-duct diffuser [1]

3.2 Grid generation

The CFD grid is generated automatically by the commercial software GridPro [17]. GridPro creates a multiblock structured grid specially under the topology paradigm. That is, if the topology (consisting of corners and edges) that fills the internal space inside the S-duct surface is built by a user at one time as shown in Fig. 4, GridPro conforms the boundary of the S-duct surface and generates the grid automatically. A user only has to pay attention to updating the new S-duct surface data during the design optimization. The S-duct geometry was normalized by the inlet diameter and the first wall distance was 10^{-5} to the normal direction so the nondimensional first-cell distance is set to around one. The inlet grid of the S-duct is shown in Fig. 5. The total grid size was 80 cells streamwise and 32 cells circumferential and a total of 151040 cells.

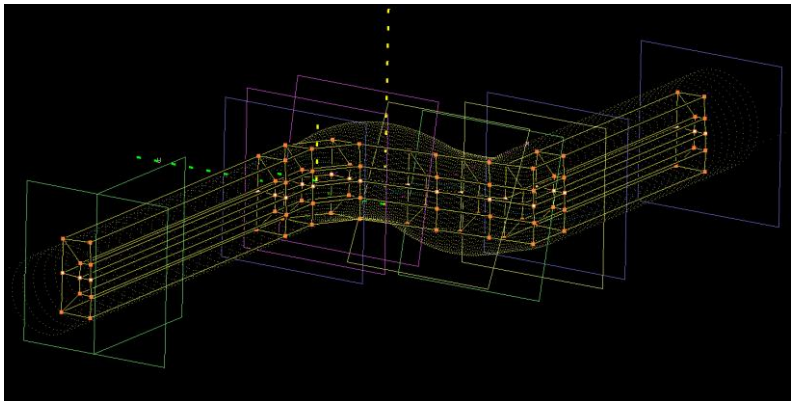

Fig. 4 GridPro topoloy for S-duct

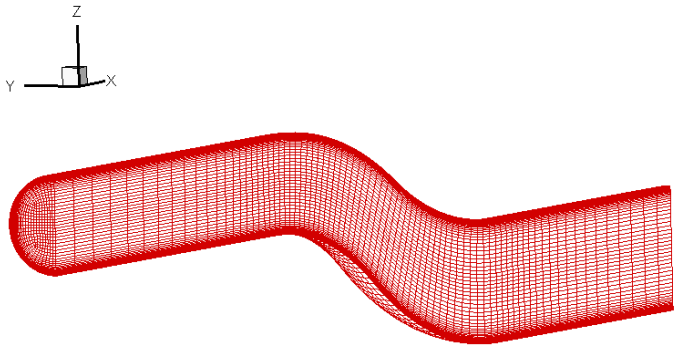

Fig. 5 S-duct grid

3.3 CFD analysis

S-duct CFD analysis was conducted by the in-house parallelized Reynolds-averaged Navier-Stokes equation code, KFLOW [18]. The time integration was done by the diagonalized alternating direction implicit (ADI) method. Spatial numerical flux was discretized using Roe's flux difference splitting (FDS) and high-ordered by 3rd monotone upstream-centered schemes for conservation laws (MUSCL). The Harten entropy correction function was used to prevent the non-physical expansion wave. The $k-\omega$ SST turbulence model which has a good performance for the flow separation and secondary flow was used [19].

For boundary conditions, the no-slip condition was applied to the wall and the Riemann invariants were used for the inlet boundary [5]. The static pressure provided from the experiment was fixed at the entire outlet boundary surface, but that static pressure was updated iteratively to meet the target mass flow rate $\dot{m}_{tar}$ at the outlet by a simple Bernoulli equation as given in equation (20) [20].

$$p_{ave} + \frac{1}{2}\rho_{ave}V^2 = p_{tar} + \frac{1}{2}\rho_{ave}V_{tar}^2 \tag{19}$$

$$p_{tar} = p_{ave} + \frac{(\dot{m}^2 - \dot{m}_{tar}^2)}{2\rho_{ave}A^2} \tag{20}$$

where p_{ave} is the average static pressure at the outlet, $\dot{m}$ is the mass flow rate at the outlet, A is the area of outlet and $\dot{m}_{tar} = \rho_{ave}AV_{tar}$.

The inlet flow conditions were the centerline Mach 0.6, Reynolds number $2.6\text{x}10^6$ based on the inlet diameter and boundary layer thickness of about 7% of the radius at the reference point (plane A) [1]. A total of eight Intel x64 Quad CPU 2.93 GHz and 30 cores in those CPUs were used for the present parallel computing. In Table. 1 the grid dependency was checked with three different grids until the L_2 norm of density was converged up to 10^{-5} as shown in Fig. 6. To take into account the wall time 'Sduct-1' grid was chosen for this study.

Table. 1 Check of grid dependency

Grid Name	Circumferential Cells	Streamwise Cells	Total Cells	PR	DC60	Wall Time(hour)
Sduct-1	32	80	151040	0.9735	0.6505	about 0.4
Sduct-2	64	160	614400	0.9777	0.6994	about 1.4
Sduct-3	96	240	1451520	0.9714	0.6352	about 2.4

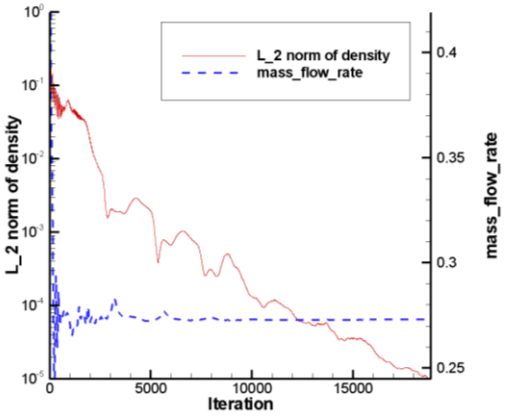

Fig. 6 Density L2 norm and outlet mass flow rate

Fig. 7 presents the surface static pressure coefficient according to the arc length. The top, side and bottom of the S-duct are at $\phi = 10^{\circ}, 90^{\circ}, 170^{\circ}$ respectively. The static pressure coefficient is defined as equation (21).

$$Cp = \frac{p_0 - p_{cl}}{p_{0,cl} - p_{cl}} \tag{21}$$

where $p_{0,cl}$ and p_{cl} are the inlet centerline total pressure and static pressure. As shown in Fig. 7, the CFD results were in good agreement with the experiments up to the first bent (s/D=2) of the S-duct due to no flow separation. After passing the first bent, the flow separated and a cross flow occurred near the surface by the centrifugal force effect and diffusing effect. Therefore, the CFD results slightly differed from the experiment in the separation region, but all the trends of the pressure coefficient followed the experiment.

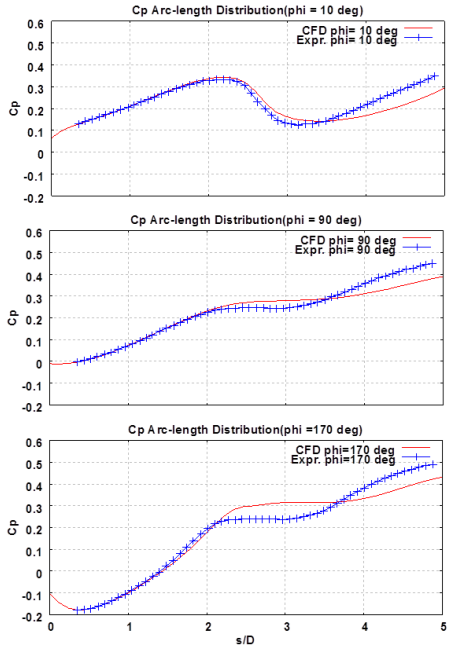

Fig. 7 Arc distribution of surface static pressures for three circumferential positions

The surface streamline was compared with the visualized experiment qualitatively [1] and the secondary flow looks similar to the measured one as presented in Fig. 8.

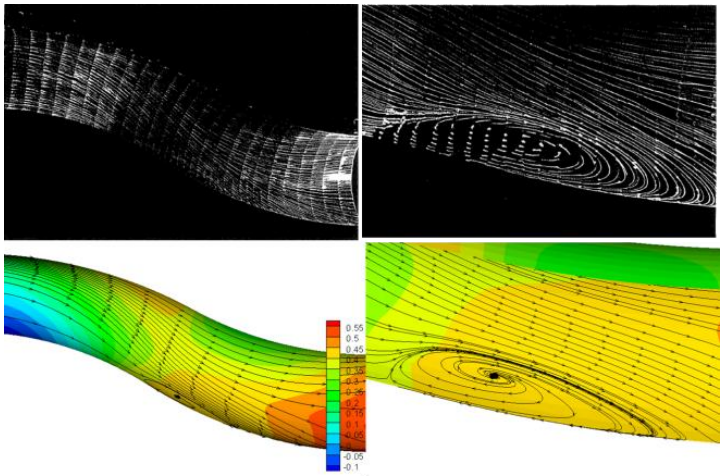

Fig. 8 Surface streamline : measured (up) and analyzed (down)

In conclusion, the baseline S-duct was analyzed to obtain the total pressure recovery (PR) 0.9735 and the distortion coefficient (DC60) 0.6505. The PR and DC are defined in detail in section 4.

4 Design Objectives and Variables

The EGO method was applied to the expensive CFD black box problem, the diffusing S-duct shape design. As the design objective functions, the total pressure recovery ratio (PR) and the distortion coefficient (DC) are defined in equations (22) and (23) [8]. If there is little energy loss in the S-duct, PR is closer to one. The DC is a measure of the non-axis-symmetry of the outlet flow. The DC becomes small as the flow progresses uniformly.

$$\mathrm{PR} = \frac{\bar{p}_{0,\mathrm{outlet}}}{\bar{p}_{0,\mathrm{inlet}}} \tag{22}$$

$$\mathrm{DC}(\psi) = \max_{0 \le \phi \le 2\pi} \frac{[\bar{p}_0 - \bar{p}_0(\phi,\psi)]}{\bar{q}} \tag{23}$$

$$\bar{p}_0(\phi,\psi) = \frac{\int_0^{\psi}\int_0^{R} p_0(r,\phi+\theta)\,r\,dr\,d\theta}{\int_0^{\psi}\int_0^{R} r\,dr\,d\theta} \tag{24}$$

where p_0 is the total pressure, $\bar{p}_0$ is the mean total pressure at the outlet and $\bar{q}$ is the mean dynamic pressure at the outlet. The ϕ of term $\bar{p}_0(\phi,\psi)$ is the starting angle of a pie-shaped slice of ψ over which the total pressure is integrated as shown in Fig. 9. Previous studies showed that design results were similar for different values of ψ [4]. In this study, DC60 was used with $\psi = 60^{\circ}$.

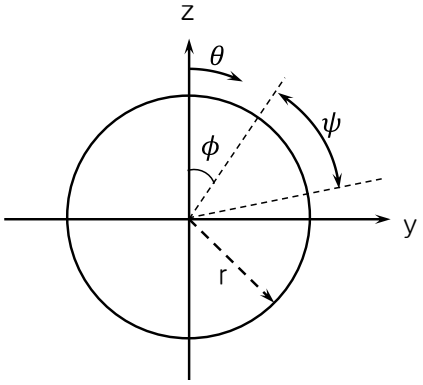

Fig. 9 Pie-slice used to calculate the distortion coefficient

In this study, only the total pressure recovery is maximized. The DC was calculated but not used for designing directly. To convert the problem into a minimization problem, the PR is multiplied by the negative sign. Equation (25) is a simple unconstrained problem. The design variable β_k is a side constraint.

$$\begin{aligned} &\max\ PR \rightarrow \min\ -PR \\ &-0.1 \leq \beta_k \leq 0.1 \end{aligned} \tag{25}$$

The radius r(x) of the S-duct was controlled by the Hicks-Henne bump function $f_k(x)$. The design variables β_k are the factor multiplied by the Hicks-Henne as shown in Fig. 10.

$$r_{new}(x) = r_{old}(x) + \sum_{k=1}^{5} \beta_k f_k(x) \tag{26}$$

$$\begin{aligned} f_k(x) &= \sin^3(\pi x^{\ln(0.5)/\ln(x_k)}) \\ x_k &= {}^1/_6, {}^2/_6, {}^3/_6, {}^4/_6, {}^5/_6 \end{aligned} \tag{27}$$

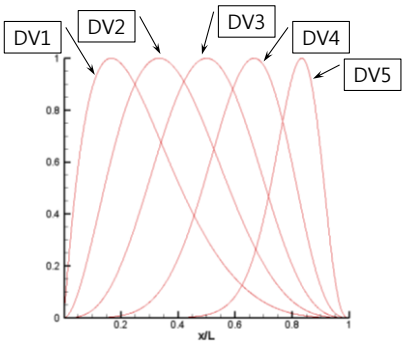

Fig. 10 Hicks-Henne bump functions

Fig. 11 shows the exaggerated shape change of the S-duct by twice the maximum design variables to account for the effect of design variable.

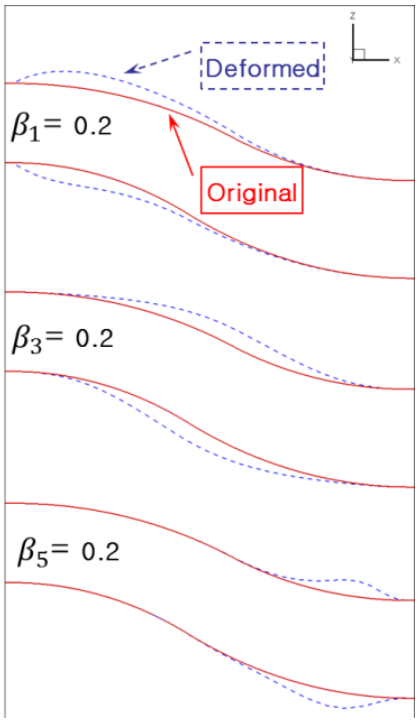

Fig. 11 S-duct shape change due to design variables

By the local sensitivity analysis for the total pressure recovery, the significant design variables were investigated and chosen. In Table. 2 DV1 has a positive largest sensitivity and DV5 has a negative largest sensitivity. So DV1 and DV5 were chosen to make the problem 2-dimensional and simple.

Table. 2 Local sensitivity for pressure recovery

	PR	Sensitivity
Baseline	0.9734	-
DV1=0.05 only	0.9875	0.282
DV2=0.05 only	0.9845	0.222
DV3=0.05 only	0.9789	0.110
DV4=0.05 only	0.9727	-0.014
DV5=0.05 only	0.9673	-0.122

Before starting to design, the true design space was plotted through 7x7 CFD runs and the true solution was searched for by the gradient-based optimizer Design Optimization Tools (*DOT*), version 4.00 [21] as shown in Fig. 12. The BFGS (Broyden-Fletcher-Goldfarb-Shanno) method was used for the *DOT* search direction. In detail the points at which DV1 is equal to -0.1 are infeasible points because the target mass flow rate as the outlet boundary condition was not achieved at those points.

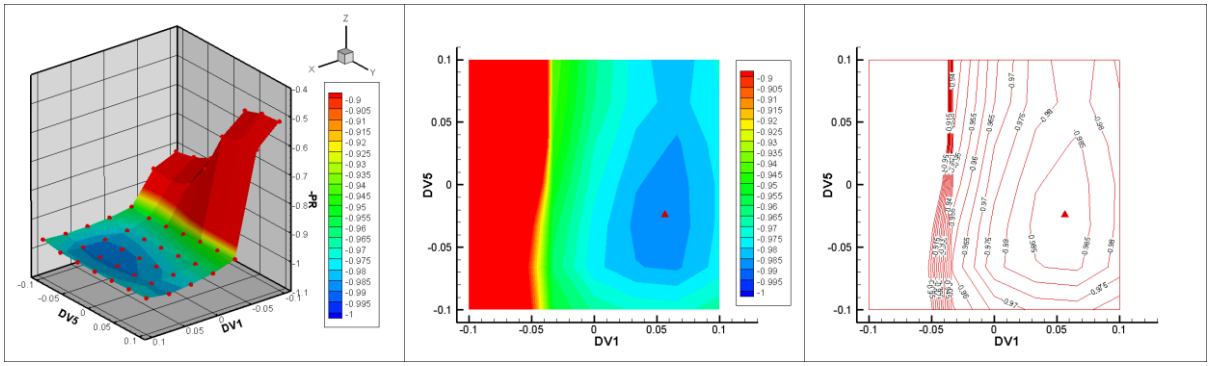

Fig. 12 Design space and true solution

5 Design Results

5.1 Results by EGO method

The initial DOE (Design of Experiment) consisted of 3x3 points noted as the circle in Fig. 13. And two kinds of stop criteria were used for the EGO method as shown in Table. 3. One is the relative EI. That is, when the relative EI (=max EI/abs($Y_{min} - Y_{max}$)) is smaller than 0.0005 and this situation occurs the number of design variables plus one times, the EGO process terminates [25]. Here Y_{min} is the smallest response value among the sampled points. Y_{max} indicates the largest response value among the sampled points. Another stop criterion is that one sampled point is located within 1% design space at the current best optimum.

In Fig. 13 the exploration of the solution was denoted as x mark. Even though EI or WB2 were used as the ISC function, the EGO method could search for the solution near the true solution. Especially WB2 explored the design space locally in the neighborhood of the true solution. In Fig. 14 the CFD run and objective change are compared with the gradient-based optimizer *DOT*. Despite of the global optimization the EGO methods (EI & WB2) needed the number of CFD run as similar as the *DOT* needed. Also the objective change by EGO is almost same to that by the *DOT*. In Table. 3 the initial objective (= total pressure recovery) was 0.9735 and the designed objective was about 0.988. It means the solution accuracy by EGO is almost same level of the gradient-based optimizer.

As the designed results by EI or WB2 are almost same, the physical results by EI are noted below. The designed S-duct shape was shown in Fig. 15. The duct diameter after the inlet became larger and the duct diameter in front of the outlet became smaller. The large inlet diameter makes an effect such that the radius of curvature of the S-duct bend becomes large. So the centrifugal force applied to the fluid passing the bend became weak and the cross-stream pressure gradient became small. As a result the lower surface pressure ($Cp = (p - p_\infty)/(0.5\rho_\infty u_\infty^2)$) became higher than the original as shown in Fig. 16. Then the streamwise adverse pressure gradient on the lower surface became so small that the boundary layer separation and the reverse flow were reduced as shown in Fig. 17. Because the energy loss by the separation was reduced, the total pressure ($Cp_0 = (p_0 - p_\infty)/(0.5\rho_\infty u_\infty^2)$) at the outlet became large as shown in Fig. 18. The low total pressure area became smaller than the original.

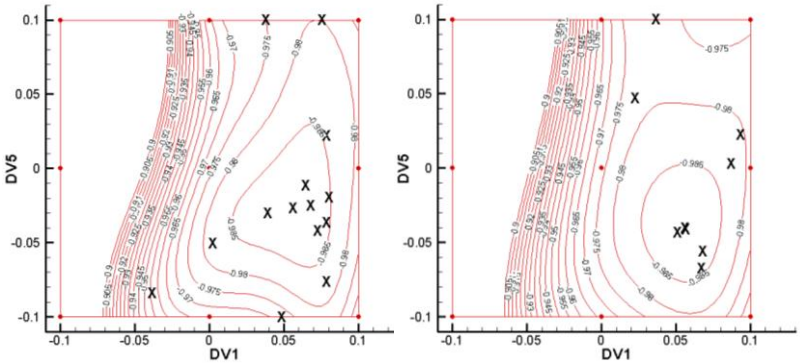

(a) EI (b) WB2

Fig. 13 Exploration of the solutions by EGO

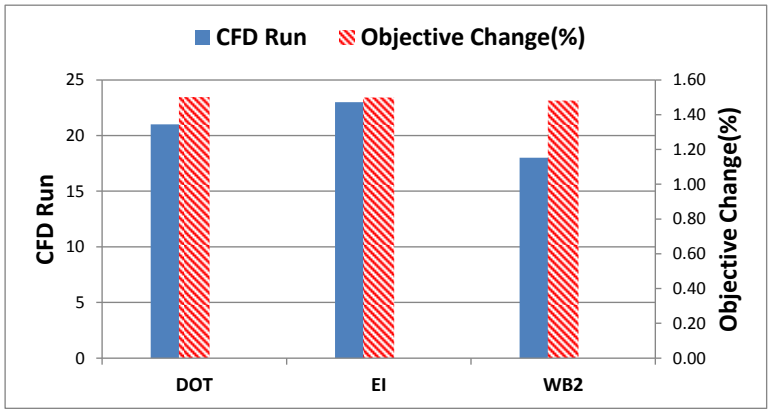

Fig. 14 CFD run and objective change by EGO

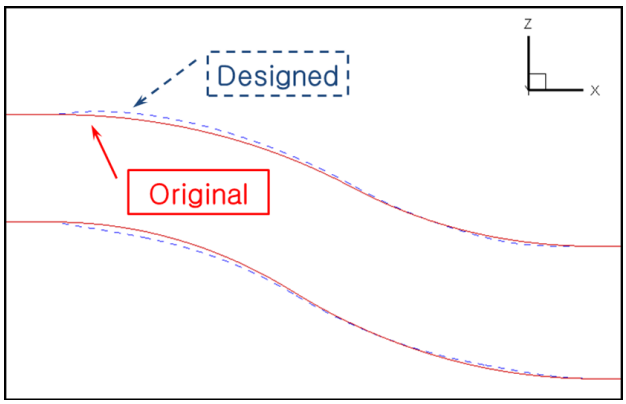

Fig. 15 Designed S-duct shape

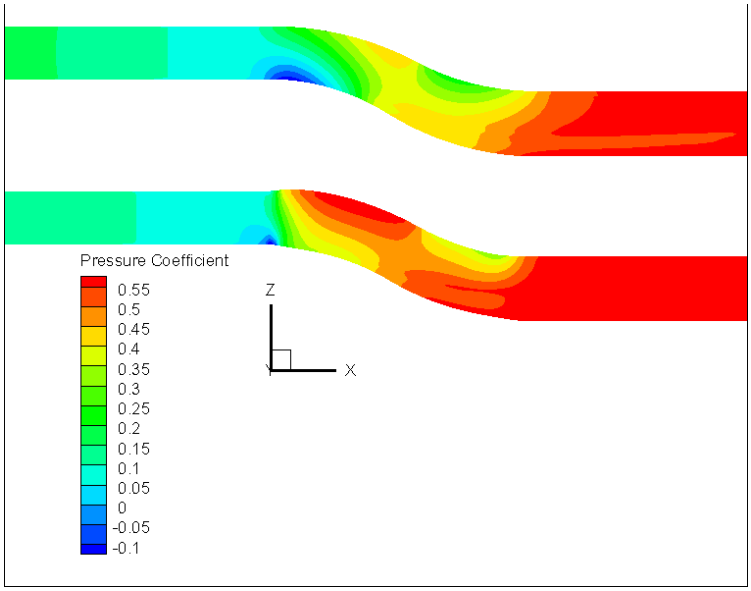

Fig. 16 Static pressure at symmetric plane : original(up) and designed(down)

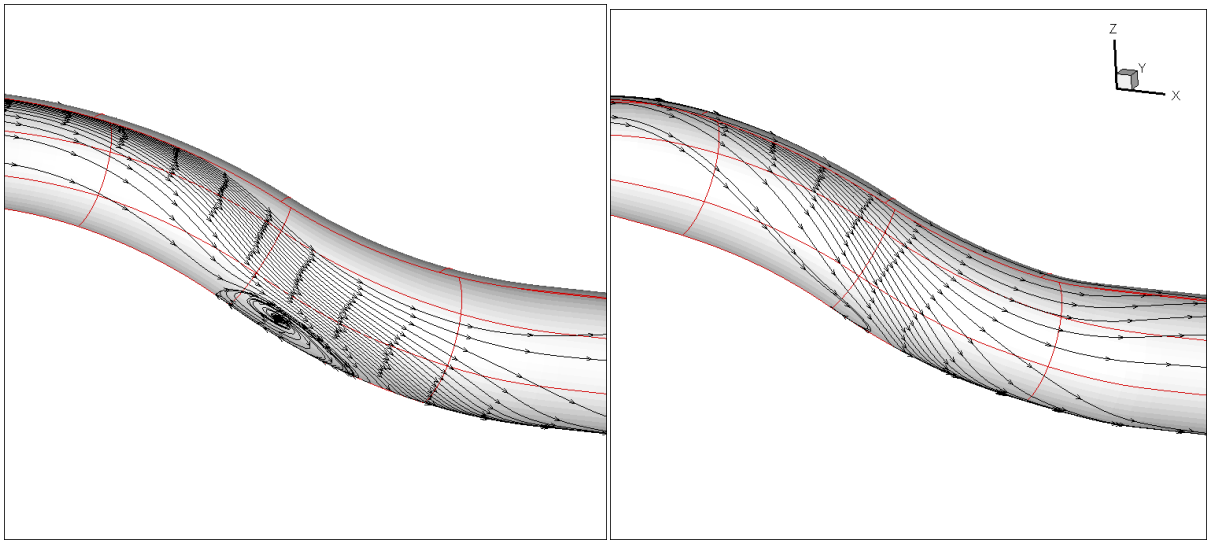

Fig. 17 Surface streamline : original(left) and designed(right)

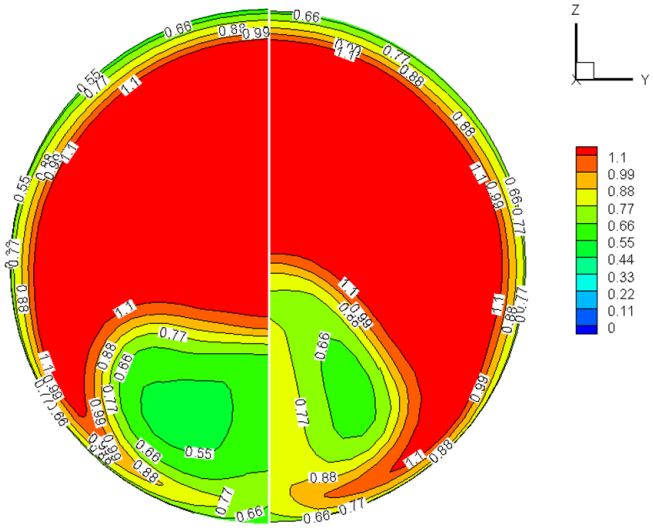

Fig. 18 Outlet total pressure coefficient : original(left) and designed(right)

5.2 Results by EGO with the penalized imputation

As the design space was investigated in section 4, the points at which DV1 is equal to -0.1 are infeasible points. Those infeasible points were replaced with the penalized imputed value and the EGO process (EI) kept going with the imputed value.

In Fig. 19 and 20 the exploration of the solution was compared when the penalized imputation was considered or not. The triangle denotes the imputed point. The non-physical pressure recovery was presented with very small value (a) EI in Fig. 19 but those disappeared (b) Penalized Imputation in Fig. 19. Also when considering the penalized imputation the next samples were selected near the true solution many times as shown in Fig. 20. The number of CFD runs and objective change were similar to the EGO method without the penalized imputation as shown in Fig. 21.

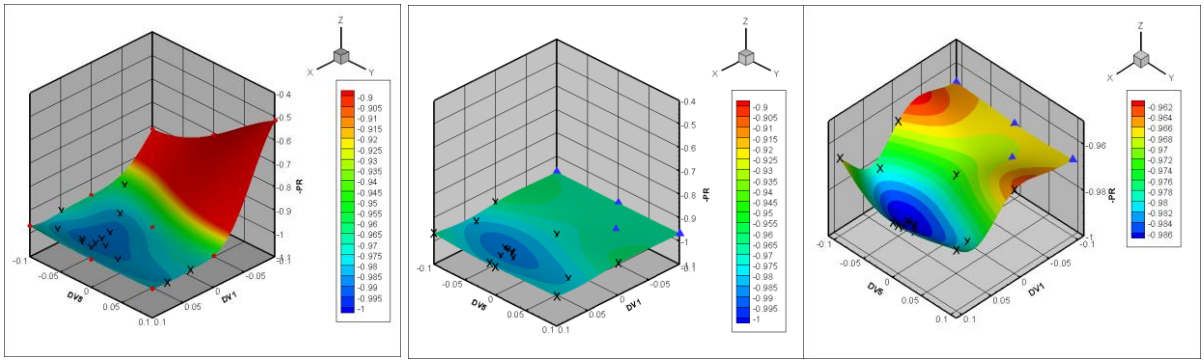

(a) EI (b) Penalized Imputation (b) Penalized Imputation(zoomed)

Fig. 19 Exploration of the solutions by EGO with the penalized imputation (3-D)

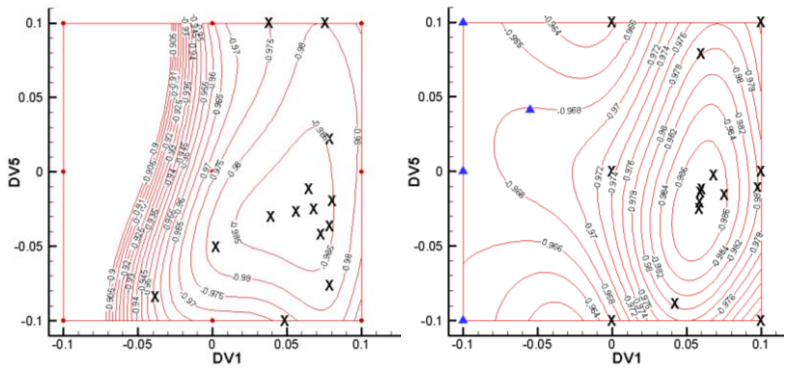

(a) EI (b) Penalized Imputation

Fig. 20 Exploration of the solutions by EGO with the penalized imputation (2-D)

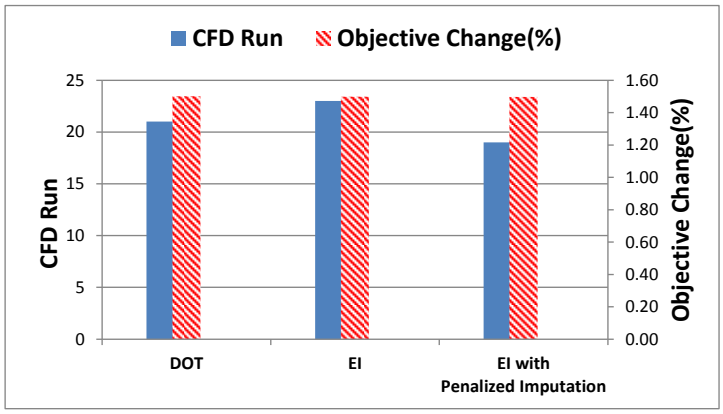

Fig. 21 CFD run and objective change by EGO with the penalized imputation

Table. 3 Summary of EGO results

		DOT	EI	WB2	EI with Penalized Imputation
Stop Criteria	REI < 0.0005 [b]	a)	v		v
	One Sample within Tolerance [c]			v	
No. of Initial DOE		21	9		
No. of Infill Sample			14	9	10
No. of Total Sample			23	18	19
Initial Objective		9.73500E-01			
Designed Objective		9.88115E-01	9.88091E-01	9.87916E-01	9.88066E-01
Change(%)		1.50	1.50	1.48	1.50
Design Variables	DV1	5.63873E-02	5.64166E-02	5.63858E-02	5.86721E-02
	DV5	-2.40955E-02	-2.65418E-02	-4.04445E-02	-2.52165E-02

a) DOT Convergence : Absolute change of objective = 9.73472E-5, Relative change of objective = 1.0E-3

b) Relative EI = max EI/abs(Ymin - Ymax) < 0.0005 and meet this criterion (no. of design variable+1) times

c) One sample is located within 1% design space of the current best optimum

6 Conclusions

The EGO method is the way to search for the global minimum efficiently for the expensive black box function such as CFD. In this study the optimal S-duct shape was determined by the EGO method and the results were compared with the gradient-based optimizer *DOT*. The EGO method achieved to improve the total pressure recovery in a similar number of CFD runs as the *DOT* did. The EGO process was stopped appropriately using two stop criteria. These results confirm the effectiveness of EGO method for the S-duct shape design.

Also the penalized imputation applied to the points at which the target mass flow rate was failed to meet. Using the penalized imputation method the exploration of the solution was more concentrated on the neighborhood of the true solution than the EGO with the infeasible points.

References

[1] S. R. Wellborn, B. A. Reichert and T. H. Okiishi. An Experimental Investigation of the Flow in a Diffusing S-Duct, AIAA/SAE/ASME/ASEE 28th Joint Propulsion Conference and Exhibit, Nashville, TN July 6-8, 1992, AIAA-92-3622.

[2] G. J. Harloff, B. A. Reichert and S. R. Wellborn. Navier-Stokes Analysis and Experimental Data Comparison of Comparison of Compressible Flow in a Diffusing S-Duct, AIAA Paper No. 92-2699, 1992.

[3] G. K. Cooper. The Parc Code: Theory and Usage, Arnold Engineering Development Center TR-87-24, Tullahoma, TN, Oct. 1987.
[4] W. Zhang, D. D. Knight and D. Smith. Automated Design of a Three-Dimensional Subsonic Diffuser, Journal of Propulsion and Power, Vol. 16, No. 6, 2000, pp. 1132-1140.
[5] W. Zhang. Three-Dimensional Subsonic Diffuser Design Optimization and Analysis, Ph.D Dissertation, Dept. of Mechanical and Aeronautic Engineering, Rutgers Univ., New Brunswick, NJ, May 1999.
[6] S. Lefantzi and D. D. Knight. Automated Design Optimization of a Three-Dimensional S-Shaped Subsonic Diffuser, Journal of Propulsion and Power, Vol. 18, No. 4, July-August 2002.
[7] B. J. Lee and C. Kim. Automated Design Methodology of Turbulent Internal Flow Using Discrete Adjoint Formulation, Aerospace Science and Technology, Vol. 11, 2007, pp. 163-173.
[8] A. Aranake, J. G. Lee, D. Knight, et al. Automated Design Optimization of a Three-Dimensional Subsonic Diffuser, Journal of Propulsion and Power, Vol. 27, No. 4, July-August 2011.
[9] R. C. Morgans, A. C. Zander, C. H. Hansen and D. J. Murphy. EGO shape optimization of horn loaded loudspeakers, Optimization and Engineering, 2008, 9, pp. 361-374.
[10] M. J. Sasena, M. Parkinson, M. Reed, P. Y. Papalambros and P. Goovaerts. Adaptive Experimental Design Applied to an Ergonomics Testing Procedure, ASME DETC Conf., ASME Paper No. DETC2002/DAC-34091, 2002.
[11] D. R. Jones, M. Schonlau and W. Welch. Efficient global optimization of expensive black-box functions, Journal of Global Optimization, 1998, 13, pp. 455-492.
[12] T. H. Lee and J. J. Jung. Chapter 16 Kriging metamodel Based Optimization, Optimization of Structural and Mechanical Systems, Jasbir S. Arora, World Scientific, 2007.
[13] J. Sacks, W. J. Welch, T. J. Mitchel and H. P. Wynn. Design and Analysis of Computer Experiments, Statistical Science, Vol. 4, No. 4, Nov., 1989, pp. 409-423.
[14] M. J. Sasena. Flexibility and Efficiency Enhancements for Constrained Global Design Optimization with Kriging Approximations, Chapter 4, Ph. D Dissertation, Dept. of Mechanical Engineering, U of Michigan, 2002.
[15] T. W. Simpson. A concept exploration method for product family design: Appendix A, Ph. D Dissertation, Dept. of Mechanical Engineering, Georgia Institute of Technology, 1998.
[16] N. L. Soren, B. N. Hans and S. Jacob. DACE, A Matlab Kriging Toolbox version 2.0, August 2002, Technical Report IMM-TR-2002-12, Technical University of Denmark.
[17] www.gridpro.com
[18] C. H. Sung, S. H. Park and J. H. Kwon. Multigrid Diagonalized-ADI Method for Compressible Flows, 31st AIAA CFD Conf., AIAA Paper 2001-2556, Anaheim, CA, USA, June 11-14, 2001.
[19] S. H. Park and J. H. Kwon. Implementation of k-ω Turbulence Models in an Implicit Multigrid Method, AIAA Journal, Vol. 42, No. 7, July 2004.
[20] FLUENT 6.3 User's Guide, chapter 7.8.4
[21] www.vrand.com
[22] A. I. J. Forrester, A. Sobester and A. J. Keane. *Engineering Design via Surrogate Modelling, A Practical Guide, Wiley*, 2008.
[23] N. Hoyle. Automated Multi-Stage Geometry Parameterization of Internal Fluid Flow Application, Degree of Doctor of Philosophy, School of Electronics and Computer Science, University of Southampton, 2006.

[24] A. I. J. Forrester, A. Sóbester and A. J. Keane. Optimization with missing data, Proceedings of the royal society A , No. 462, pp.935-945, 2006.
[25] D. Huang, T. T. Allen, W. I. Notz and N. Zheng. Global Optimization of Stochastic Black-Box Systems via Sequential Kriging Meta-Models, Journal of Global Optimization, Vol. 34, Issue 3, pp.441-466, 2006.

APPENDIX

Notation

Cp static pressure coefficient
DC distortion coefficient
DV design variable
EI expected improvement
WB2 Watson and Barnes type 2
f_{min} minimum response of all sample points
PR total pressure recovery
R correlation function
R correlation matrix
s sample point
x untried point
Y response vector of sample points
$\hat{Y}$ mean value of kriging model (= predictor)
$\hat{s}^2$ mean square error of kriging model
θ correlation parameter
$\boldsymbol{\theta}$ correlation parameter vector
Φ cumulative distribution function (CDF)
ϕ probability density function (PDF)